Investigation of Gate Rudder Blade Design for Ship Powering Using the Design of Experiment (DoE) Method

Ahmet Yusuf Gurkan[1,2], Batuhan Aktas[2], Uğur Oral Unal[1], Mehmet Atlar[2]

[1]*Faculty of Naval Architecture and Ocean Engineering, Istanbul Technical University, 34469, Maslak – Istanbul – Turkey*
[2]*Naval Architecture, Ocean & Marine Engineering, University of Strathclyde Glasgow G4 0LZ, UK*

Abstract

The Gate Rudder System (GRS) is a novel steering and energy-saving device that has proved itself on the first newbuilt container vessel, "Shigenobu" in 1998, followed by three other newly built vessels operating in the coastal regions of Japan. Although there is a clear indication that these vessels with GRS presented attractive powering savings based on different scale model tests, sea trials and voyage monitoring, no comprehensive investigation has been reported in the open literature so far describing the best-performing GRS design. This paper presents a geometric sensitivity study, the best design selection procedure for a GRS, and its application to a 90m general cargo vessel (MV ERGE) from the powering performance point of view. MV ERGE is the target ship used in the H2020 project GATERS (ID: 860337) which aims to design and demonstrate the benefits of retrofitting a GRS system on a full-scale ship.

In this paper, a Design of Experiment (DoE) study was performed with a wider range of design space to investigate the sensitivity of the chosen design variables by focusing on the powering performance. The computational Fluid Dynamics (CFD) method was used to calculate each design point flow variable. Based on the application, the most effective geometrical parameter was determined to be the rudder angle from the correlations made between the input and output parameters. Further scrutinisation of the input parameters vs output parameters indicated that the best powering performance was not achieved with the highest rudder force (thrust). Instead, the best GRS design could be obtained by achieving the most favourable interaction amongst the propeller, hull and GR blades to maximise the overall energy saving. For further verification, a comprehensive comparison was made using further high-fidelity CFD modelling of the propeller action.

Keywords: Energy-saving device; Gate Rudder System; Optimisation; Design of Experiment; Computational Fluid Dynamics.

1 Introduction

In order to contribute to the global fight against climate change, IMO announced varying levels of regulations to meet CO_2 emission reduction by ships at least 40% by 2030, pursuing efforts towards 70% by 2050 compared to 2008 (IMO, 2018). Hence, many technology solutions have been proposed to address this challenge. The applications of the proposed solutions range from newbuilt ships to existing ships as a retrofit, from individual solutions to holistic ones, and from existing technologies to newly introduced ones. For example, the recent H2020 project GATERS (INEA et al., 2020) (ID: 860337), aims to exploit the application of a novel propulsion and manoeuvring energy-saving device (ESD) called "Gate Rudder System" (GRS) that provides a sound base for the most attractive power-saving hence reduced emission option (Sasaki, et al., 2015). More specifically, GATERS aims to design, manufacture and install a retrofit GRS on a general cargo vessel MV ERGE and prove the effectiveness of the new technology through sea trials and voyage monitoring. Additionally, GRS's powering, seakeeping and manoeuvring benefits for a wider range of ship types, including Short Sea Shipping (SSS) and Oceangoing Shipping (OS) operations are being explored in the GATERS project.

As shown in Fig. 1, a GRS involves the arrangement of a twin rudder system differently than a conventional rudder system (CRS) by replacing the single rudder behind the propeller with the independently controlled twin rudders aside from the propeller. This novel arrangement has many advantages compared to the CRS. A comprehensive investigation of the early version of the GRS, called the twin rudder system, was made for the first time by Sasaki et al. (2015). Based on the first measurements, it was understood that the state-of-the-art GRS has a number of superiorities over a high lift rudder on propulsion

(Turkmen et al., 2016), manoeuvrability (Carchen, et al., 2016) and seakeeping capabilities (Sasaki, et al., 2019).

The first GRS application was made to a newly built container ship, "Shigenobu". Her sister ship, "Sakura", with a conventional high lift rudder (CRS) was enabled to make comprehensive performance comparisons through numerous sea trials and voyage monitoring since 2018. The collected performance data in the first sea trials indicated that Shigenobu had 14% lower energy consumption at the design speed than Sakura. A further energy saving was also observed in rough sea conditions, where Shigenobu's energy efficiency could be as high as 30% (Sasaki et al., 2020).

Although there are clear indications of the energy-saving capabilities of the GRS based on model tests and full-scale monitoring, there are no detailed investigations of the GRS that would provide a further understanding of the effect of some important GRS design parameters on the hydrodynamic interaction amongst the hull, propeller and gate rudder blades, and powering performance of a vessel with a GRS.

Fig. 1. Shigenobu, the first Gate Rudder System fitted ship

Therefore, this paper aims to provide systematic design data for GRS based on the calm water powering performance by conducting a comprehensive Design of Experiment (DoE) study by creating the fully parametric design of a GRS and mainly concentrating on the vertical part of the rudder blades. Parametric model preparation and the DoE study were performed within an optimisation-based CAD software environment called CAESES (FSYS, 2022). The parametric gate rudder model was prepared over four geometrical design variables, which control only the vertical part of the Gate Rudder blade.

The detail of the definitions of each parameter and general geometrical constraints are presented in Section 2 of the paper. In order to evaluate the powering performance of the ship, RANS-based Computational Fluid Dynamics (CFD) calculations were conducted for each design point created in the design space with the commercial CFD solver Star CCM+ (StarCCM+, 2022). The details of the CFD methodology used for the verification & validation, sensitivity analysis and design validation study are given in Section 3 of the paper.

The particulars of both the target vessel MV ERGE and the benchmark vessel, Shigenobu, used for the validation and verification are given in Table 1. Validation in a full-scale ship was performed with the extrapolated data. In order to realise optimisation within a reasonable run time, some simplifications were made on both the propeller modelling approach and the computational domain. Although the Virtual Disk (VD) model approach was used to evaluate the propulsion performance for the DoE study, the calculated average forces for verification in Section 3.4 and design validation in Section 5.3 were made by using the rigid body motion of the propeller using the sliding mesh (SM) model approach.

In order to derive the correlations between the design variables versus some hydrodynamic parameters, a design space should be solved over the nodes represented by the design points. For this purpose, the "Sobol" approach was employed for the design space generation. The Sobol algorithm (Sobol, 1967), which is an example of a quasi-random low-discrepancy sequence, creates random design points evenly distributed within the design space. The theoretical background of the Sobol sequence and detail of the sensitivity study is given in Section 4 of the paper.

Table 1. Ships particulars

		ERGE Ship	**JCV Ship**	**JCV Model**
Scale, m	λ	1	1	10.938
Length Over All, m	L_{OA}	89.95	111.4	10.110
Length Between perp., m	L_{BP}	84.95	101.9	9.316
Breadth, m	B_{WL}	15.40	17.80	1.627
Draught (AP), m	T_A	6.46	5.51	0.504
Draught (FS), m	T_F	6.46	4.91	0.449
Displacement, ton	Δ	7462.7	6489	4.958
Block Coefficient	C_B	0.806	0.591	0.591
Service Speed, m/s	V_S	6.173	1.650	2.333
Propeller Diameter, m				
Conventional Rudder		3.42	3.5	-
Gate Rudder		3.60	3.3	0.302

The results of the applications of the algorithm are presented in Section 5, while the details of the calculated correlations between the input and output parameters are presented in Section 5.1. Rudder angle, "δ", was observed to be the most critical parameter investigated over the rudder forces, propeller thrust and delivered power

variations. Detailed performance evaluation on some selected design cases and overall relations between variables of the GRS on ship powering are discussed in Section 5.2. Finally, the best-performing GRS design was validated with the SM approach in 5.3. The concluding remarks deducted from the study are presented in Section 6 of the paper.

2 Parametric Model

In order to parametrise the GRS blades effectively and the contribution of these parameters to powering performance, it was decided to divide the GRS blade into sub-sections and examine the effectiveness of these sections in detail. These sections are described as shown in Fig. 2. Considering the interaction level of the GRS blades and the propeller, only the vertical part (the first part) of the GRS was chosen as the subject within the context of the current sensitivity study.

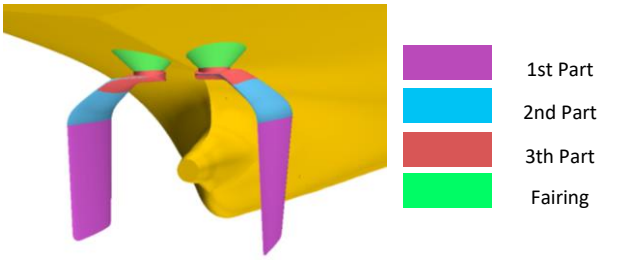

Fig. 2. Parametric model definitions

The current GRS blade called Base Design (BD) was used to create a fully parametric CAD model. Some existing characteristics of the rudder such as; blade profile shape, 2nd, 3th par of the rudder and finally fairing shape were kept same with the BD.

In the CAESES environment, four independent parameters are chosen for this study. These parameters include as the first parameter, i.e., 'Rudder angle (δ)', presenting the rotation of the whole rudder around the centre of the rudder shaft. Rudder motion and rotation direction are defined as shown in Fig. 3. The second parameter is 'Rudder X shift (dx)', the rudder's axial position relative to the propeller. The base design's relative position to the propeller was assumed to be zero. The third parameter is 'Rudder tip skewness (β)', i.e. the angle relative to the top profile of the first part of the rudder. And the last parameter is the 'Blade tip-chord ratio', which is the ratio of the blade tip chord (at the bottom) to the top chord length. Each design was prepared to have an identical rudder area equivalent to the base GRS design. Therefore, the last parameter inherently changes the aspect ratio of the rudder blade. The lower and upper bounds are listed in Table 2 for each parameter.

In order to prevent each GRS design considered would have physical contact with the propeller or hull, a limiting criterion is introduced. This is required if the rudder gets closer to the propeller boss cap less than 5% of the propeller diameter at the rudder's +110° helm position; such design will be disregarded. None of the design points is allowed to take place in the design space, which violates this rule.

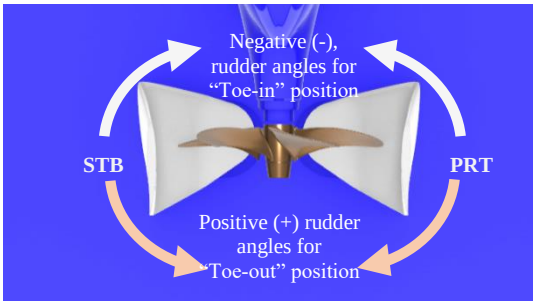

Fig. 3. Parametric model definitions

Table 2. Geometric parameters and limits

Name		Lower Band	Upper Band
Rudder angle[1], degree	δ	-6.0	6.0
Rudder X shift[2], m	dx	-0.40	0.17
Rudder tip skewness[1], degree	β	0	8
Blade tip chord ratio, -	C_T	0.68	0.74

[1] '+' sign represents toe-out direction

[2] '+' sign represents head direction of the ship

3 CFD Methodology

The theoretical background and the detail of the numerical model, such as the computational domain grid generation and discretisation of the governing equations, are given in this section.

3.1 Theoretical Background and Numerical Models

The CFD calculations were carried out via the Start-CCM+, which is a commercial viscous flow solver. The governing equations were discretised by finite-volume approach and were solved using a segregated approach.

Calculations were done using the Reynolds Average Navier-Stokes (RANS) equations in the transient domain. Multiphase calculations were done in a transient domain, while the DoE study (the calculation with simplified fluid domains) was performed in a steady-state domain.

Multiphase flow, where the free-surface effects were considered, was solved using the Volume of Fluid (VoF) approach. Regarding the turbulence modelling, Realisable k-ε was employed with all wall treatment approaches. All the multiphase calculations were performed in calm water conditions by allowing ships in two Degrees of Freedom (DoF), i.e., heave and pitch motion.

The propulsion calculations were performed in two different approaches.

The first one is the sliding mesh (SM) approach which is based on rigid body motion. The defined motion moves the mesh vertices according to user-specified rotation, translation or trajectory. Around the corresponding rotation, the centre was defined as rigid body motion Eq 1, where Vg: mesh velocity, ω_g: prescribed angular velocity, r: position vector of a mesh vertex (StarCCM+, 2022).

$$V_g=\omega_g \times r \quad (1)$$

In applying the SM method, the propeller speed should be set to the operation point where the propeller thrust is equivalent to the ship resistance, additionally considering friction drag in the model scale.

The second model adopted is the Virtual Disk (VD) model which is based upon the principle of representing rotary machinery such as propellers, turbine rotors, etc., as an actuator disk and hence, provides considerable computational time and resource-saving. The action of the actuator disk on the flow field enters the momentum equations in the form of a source term that is distributed over the virtual disk. Various distributions of different fidelity are possible to model the action of the actuator depending on the application area. "Body Force Propeller Method", which simulates the effects of a marine propeller, were used for the VD-based calculations as the actuator disk (StarCCM+, 2022).

As a result, the distribution of the axial and tangential forces of the modelled propeller and its effect on the flow is calculated. The integration of these forces over the disk gives the thrust and torque of the propeller.

Both approaches shown in Fig. 4 were performed in the validation and verification study in Section 3.4 and design validation for the best-performing GRS design is chosen from the DoE as described in Section 5.3.

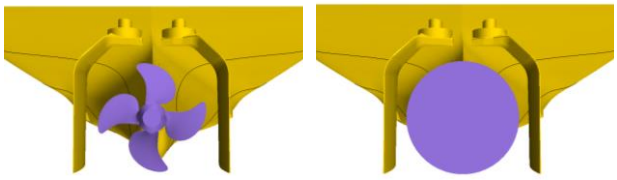

a. b.

Fig. 4. Propeller modelling approaches; a. Rigid body motion (Sliding Mesh), b. Actuator disk (Virtual Disk)

3.2 Computational Domain and Boundary Conditions

Following the ITTC recommended procedure (ITTC, 2014) for ship hydrodynamic calculations, the computational domain for CFD was prepared for both the target ship MV ERGE and benchmark vessel Shigenobu for validation study, whose dimensions are given in Table 1. Fig. 5 shows the dimensions of the general computational domain for the full-scale and model-scale ships. The fluid domains for the CFD modelling were prepared according to the ship and/or model length and they are also shown in Fig. 5. There are 2L distances between the boundaries at either side and the fore and 3L distances at the aft end of the ship, where L represents the length of the water line. The upper and lower boundaries are located at 1L and 2.5L, respectively.

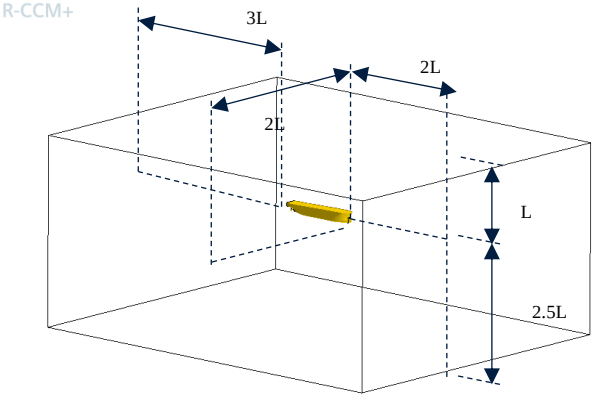

Fig. 5. Main dimensions of the computational domain.

In order to reduce the computational cost of the DoE study, the simulation simplifications were implemented over three levels, including the propulsion modelling approach. The process was performed starting from the most complex case to the simplest one, as given in Table 3. The chosen mesh structure and cell counts are given in Section 3.4.

The first level of simplification (Case 1) is on the propeller modelling approach. This case has a significant number of mesh cells, around 23 M. The existence of the propeller with the SM approach causes an additional 6.6 M over Case 2, which solves propeller interaction with the VD approach. As a result, the mesh count in Case 2 reduces by 30% relative to Case 1.

Both Case 1 and Case 2 require transient simulation because of ship motion (pitch & heave) and propeller rotation (for only Case 1). Therefore, these cases have significantly high run times (more than ten times) compared to Cases 3 & 4, as it is shown in

Table **6**.

The second simplification was made by focusing only on the underwater part of the ship. The free-surface effects were not considered for Cases 3 and 4, as shown in Fig. 6, b and c. Instead, the wave resistance is calculated from the total resistance difference between Case 2 and 3, and then the calculated wave resistance is added to the VD thrust expression and the rest of the resistance calculations. Case 3 has an additional 16% reduction in the total cell number relative to Case 2.

The last simplification was implemented in Case 4 by cutting and removing the forebody of the ship, as shown in

Fig. 6,c. In order to practice this cutting process at a convenient location, the effective stern region interacting with the propeller was determined by comparing the distribution of the pressure coefficient "C_P "and the friction coefficient C_F along the three different reference lines on the hull. These lines named the bottom (z:-0.8D from the propeller centre line), centre (z:0 propeller shaft centre), and top (z:+0.9D from the propeller centre line are shown in Fig. 8. From the graphs in Fig. 8, the propeller interacts with only the aft 15% of the ship, which is equivalent to 12.7 m. Therefore, just the aft 30 m of the ship is kept in Case 4, which is the most simplified ship domain, considering the parallel body. The detailed results are presented in Section 3.4.

As the inlet surface of Case 4's fluid domain starts from the ship cross-section, the detailed velocity (x, y and z) components were defined on the surface instead of uniformly distributed inlet velocity. These velocity and turbulence components data were derived from the corresponding cross-section in Case 3. The velocity distribution is shown in Fig. 7.

Table 3. Geometrical model detail for the simplification study

Name	Ship Detail	Propeller Detail
Case 1	Full-model	Sliding Mesh
Case 2	Full-model	Virtual Disk
Case 3	Double-model	Virtual Disk
Case 4	Clipped double-model	Virtual Disk

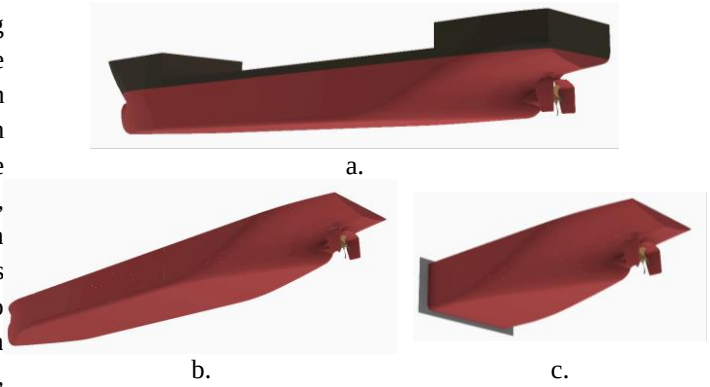

Fig. 6. Simplified fluid domains; a.Full domain, b.Double model, c.Trimmed double model

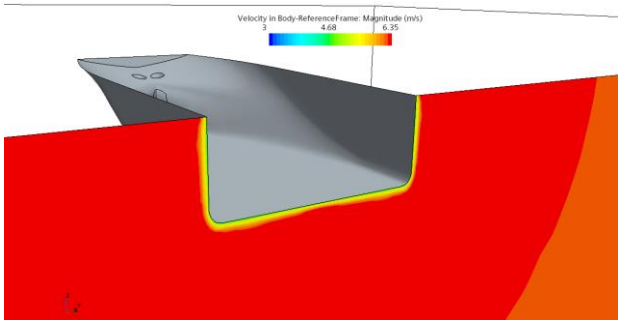

Fig. 7. The defined non-uniform velocity distribution at the inlet surface of Case 4

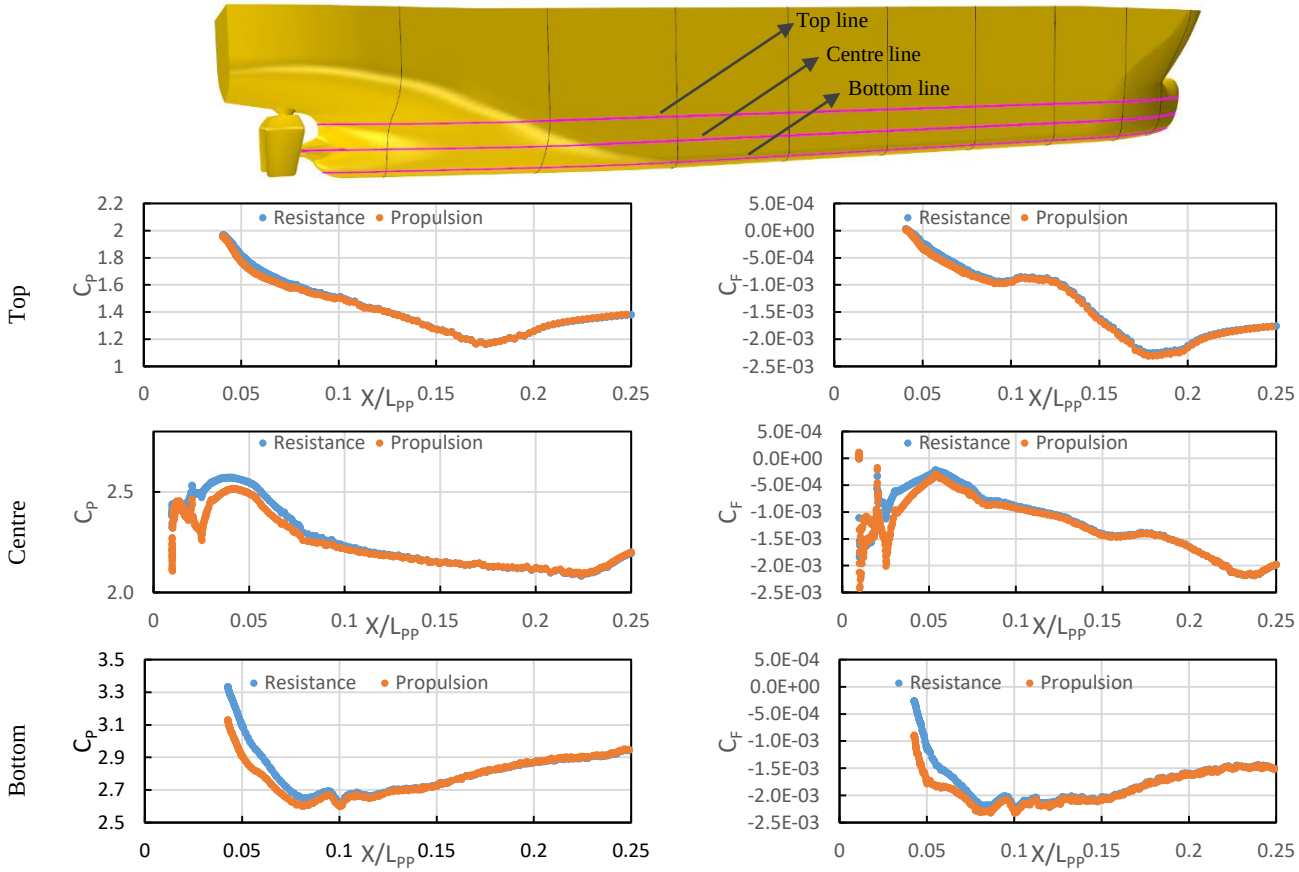

Fig. 8. Propeller-hull interaction investigation at the stern of MV ERGE over C_P and C_F

3.3 Mesh Generation and Physics Set-up

STAR CCM+ meshing tool was employed for mesh generation. The trimmer-type technique used for the surface and volumetric mesh is a hexahedral-type grid structure. In order to capture high gradient velocity normal to the walls, prism layers were defined along the wall. Further local mesh refinements have defined locations like; the bow and stern of the ship, the rudder surrounding, and the free surface to capture high gradient flow and wave evaluations.

Extra grid refinement was applied at the rudder region. In the case of self-propulsion simulation, extra grid refinement was done around the disk. For the full-scale ship calculations, there were ten layers of boundary-layer meshes near the hull, and the average wall function y+ value was kept between 30 and 60, as calculated and suggested by similar numerical studies. For the model scale calculations, there were 20 layers of boundary-layer meshes normal to the wall. The average y+ value was <1 to solve the viscous sub-layer. Calculated y+ values are shown in **Fig. 9** for both scales. The realisable k-ε turbulence model was used as the RANS closure model. The volume of fluid method (VOF) for multiphase flows was used to account for free surface effects. The model was unconstrained to move in 2 degrees of freedom (with sinkage and trim) using Dynamic Fluid Body Interaction (DFBI), allowing the simulation to attain a consistent dynamic attitude for V&V study and Case 1 & 2.

Since the free-surface effects did not include in the calculations for Case 3 & 4, no degree of freedom was allowed. Instead, the heave and pitch values calculated from Case 2 were introduced to Case 3 & 4 domains.

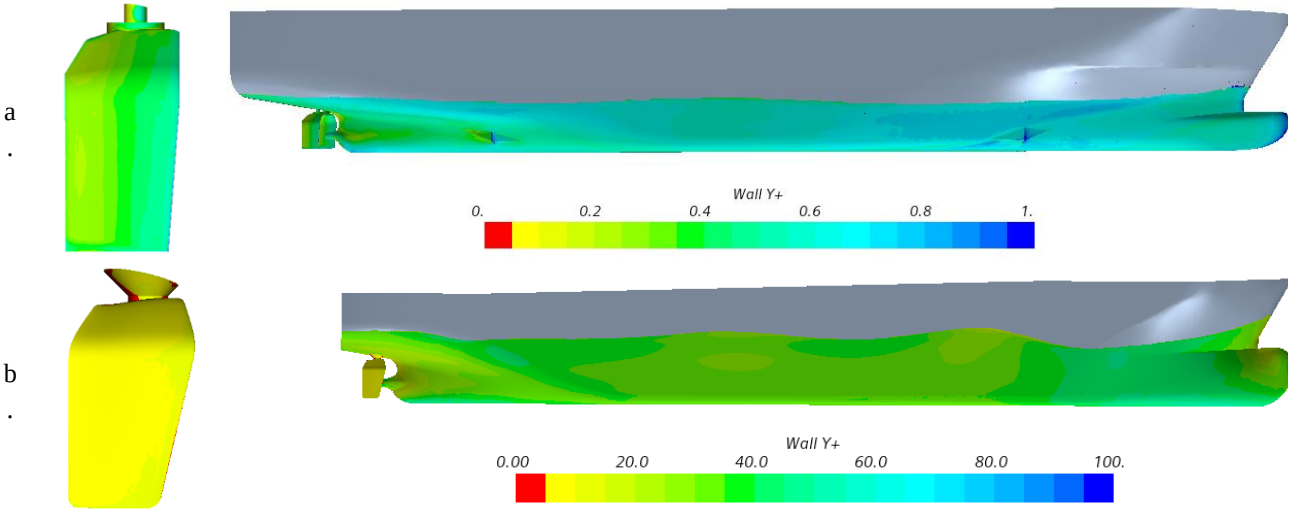

Fig. 9. Calculated y+ distribution on the hull; a.Shigenobu (validation ship), b.MV ERGE (subject ship)

3.4 Verification and Validation Study

Richards Extrapolation based Grid Convergence Index (GCI) was used to demonstrate the accuracy level of the CFD calculations (Richardson & Gant, 1927). that is based on the Richards Extrapolation (Richardson L. F., 1911; Richardson & Gant, 1927) to calculate the numerical described by (Celik et al., 2008).

GCI which are calculated using Eqs. 2 to 4, where r_{21} and r_{32} are refinement factors, $\emptyset_k$ represents the corresponding CFD output variable (resistance, thrust, torque and RPM) and $\varepsilon_{21}$and ε_{32} are the difference between the results obtained from relevant grids 1 (fine), 2 and 3 (coarse), respectively. For this study, the refinement ratio was set as ~2 for the model-scale ship and 2.2 for the full-scale ship.

$$p = \frac{1}{\ln(r_{21})} \left| \ln\left|\varepsilon_{32}/\varepsilon_{21}\right| + q(p) \right| \qquad (2)$$

$$q(p) = \ln\left(\frac{{r_{21}}^p - s}{{r_{32}}^p - s}\right) \qquad (3)$$

$$s = 1 \cdot \text{sign}\left(\frac{\varepsilon_{32}}{\varepsilon_{21}}\right) \qquad (4)$$

The extrapolated values by using associated results and refinement ratio are obtained by Eq. 5.

$$\emptyset^{21}{}_{\text{ext}} = \frac{({r_{21}}^p \emptyset_1 - \emptyset_2)}{({r_{21}}^p - 1)} \qquad (5)$$

The approximate and extrapolated errors are calculated using Eqs. 6 and 7, and the Grid Convergence Index between the two finest grids (GCI_{21}) is given by Eq. 8.

$$e_a{}^{21} = \left|\frac{\emptyset_1 - \emptyset_2}{\emptyset_1}\right| \qquad (6)$$

$$e_{ext}{}^{21} = \left|\frac{{\emptyset_{ext}}^{12} - \emptyset_1}{{\emptyset_{ext}}^{12}}\right| \qquad (7)$$

$$GCI^{21}{}_{fine} = \frac{1.25\, e_a{}^{21}}{r_{21}{}^{p} - 1} \qquad (8)$$

The GCI for both model and full-scale version of Shigenobu demonstrates the level of variation of the result relative to the grid structure. Three different mesh structures (shown in Fig. 12) were generated to perform GCI. The calculations were done for the Fr = 0.234, which corresponds to 15knots ship speed (service speed) in full scale. Performed verification study with varying mesh density demonstrated that the grid independency level is quite high for both scales. Calculated $GCI^{21}{}_{fine}$ for fundamental ship hydrodynamic variables are lower than 1%, as shown in Table 4 and In addition to the test results conducted by HSVA, the extrapolated powering results based on the model tests conducted at the ITU towing tank with a smaller model of Shigenobu (λ=21.5) model and using the ITTC'78 method were added in Fig. 11. The average difference between calculated P_E values and ITU measurements is ~1.8%, while ~11% with the HSVA measurements. Similarly, the average P_D difference between the CFD and predictions are 0.6% and 14% compared to the ITU and HSVA model test based extrapolations, respectively.

Table 5. Although $GCI^{21}{}_{fine}$ average ratio of rudder axial forces, which present the resistance forces in the model scale, are ~6%, the reason is the force values are significantly close to zero.

Based on the comparison between the CFD results and the model test results conducted in the HSVA towing tank with a model scale of λ= 10.938, the accuracy level of the best mesh (JM G1) is quite high by showing 0.8% difference from the EFD on resistance and torque. The Experimental Fluid Dynamics (EFD) results of HSVA given in Table 4 have not been published yet.

Further comparisons of the effective and delivered power results for a wide range of ship speeds are given in Fig. 10 and Fig. 11 for the model and full-scale versions of the Shigenobu, respectively.

Table 4. GCI study for the model scale JCV with gate rudder propulsion prediction; Fr:0.234 at loaded condition

	EFD	JM G1	JM G2	JM G3	$GCI^{21}{}_{fine}$	$\delta\emptyset_2$
Cell Count	-	8.6M	4.3M	2.3M	-	-
R_{TM}, N	197.3	194.0	193.4	189.1	0.0039	0.8%
T_M, N	161.5	161.6	161.0	155.9	0.0003	0.1%
Q_M,kN.m	7.15	7.20	7.19	7.02	0.0000	0.8%
n_M, rps	10.96	10.90	10.90	10.91	0.0003	0.6%
P_{Dm}, W	492.18	493.37	492.11	481.17	0.0002	0.2%
$R_{GRS\ PRT}$, N	-	1.05	1.14	1.33	0.0720	-
$R_{GRS\ STB}$, N	-	1.29	1.37	1.54	0.0468	-

In addition to the test results conducted by HSVA, the extrapolated powering results based on the model tests conducted at the ITU towing tank with a smaller model of Shigenobu (λ=21.5) model and using the ITTC'78 method were added in Fig. 11. The average difference between calculated P_E values and ITU measurements is ~1.8%, while ~11% with the HSVA measurements. Similarly, the average P_D difference between the CFD and predictions are 0.6% and 14% compared to the ITU and HSVA model test based extrapolations, respectively.

Table 5. GCI study for the full scale JCV with gate rudder propulsion prediction; Fr:0.234 at loaded condition

	JF G1	JF G2	JF G3	$GCI^{21}{}_{fine}$
Cell Count	18.0 M	8.3 M	4.0 M	hyp
R_{TS}, kN	219.2	219.3	216.1	hyp
T_S, kN	240.6	241.6	239.3	hyp
Q_S, kN.m	116.0	116.7	116.0	hyp
N_S, rpm	200.6	201.8	202.3	0.0069
P_{DS}, kW	2437	2465	2457	hyp
$R_{GRS\ PRT}$, kN	0.42	0.44	0.36	hyp
$R_{GRS\ STB}$, kN	0.00	0.35	0.13	hyp

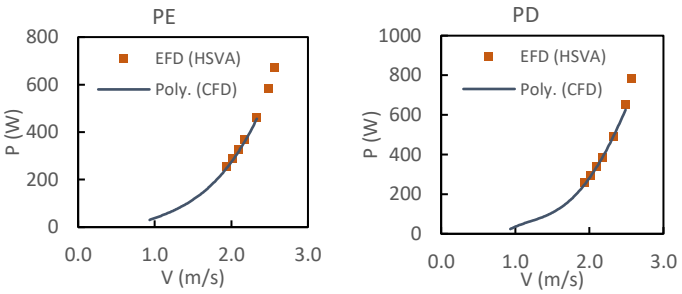

Fig. 10. Model-scale Shigenobu EFD vs CFD comparison for varying speeds

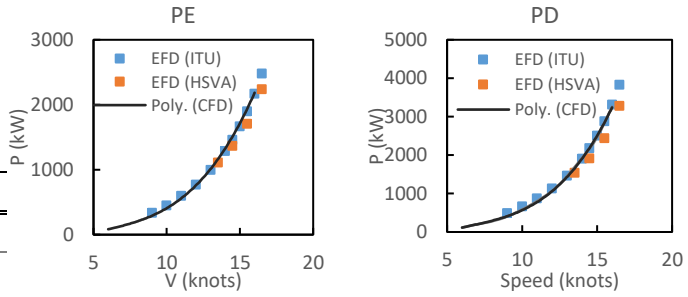

Fig. 11. Full-scale Shigenobu EFD vs CFD comparision for varying speeds

Table 6. Hydrodynamic variable comparison for fluid domain simplification

Case	Mesh Count (M)	Run Time (h)	$F_{GRS\ Prt}$ (kN)	$F_{GRS\ Strb}$ (kN)	$F_{GRS\ T.}$ (kN)	$\delta F_{GRS\ T.}$ (%)	T (kN)	Q (kN.m)	N (RPM)	P_D kW	δP_D (%)

Case 1	22.0	>160	6.31	5.10	11.40	-	188.97	93.78	136.8	1344	-
Case 2	15.4	~72	5.61	5.67	11.28	-1.1	185.80	96.17	137.0	1380	2.7
Case 3	11.9	~6	6.28	6.31	12.59	10.4	184.82	95.03	135.0	1343	0.0
Case 4	7.0	|~4	6.10	6.17	12.27	7.6	184.01	94.69	134.9	1338	-0.4

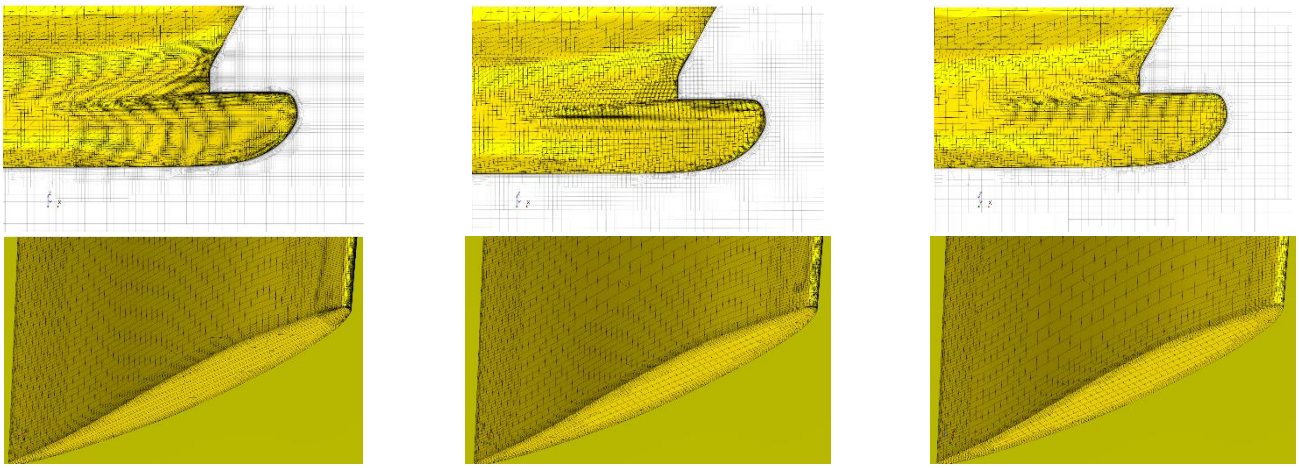

JM G1 JM G2 JM G3

Fig. 12. Three different mesh structures for model scale (λ:10.938) Shigenobu

4 Sensitivity Methodology

The Design of Experiment was conducted by using the Sobol Algorithm within the explored space that was limited by defined minimum and maximum bounds for each design variable.

The Sobol sequence sampling method used for the study is a quasi-random sequence which is the replacement of the full factorial distributed in a uniform way (Sobol, 1967).

In the Sobol sequence, two uniform partitions of the same interval are utilised, and then it reorders the coordinates in each dimension. If we let $I^S = [0,1]^S$ be the s-dimensional hypercube, and f be a real integral function over I^S, in this case, the Sobol sequence should construct a sequence x_n in I^S in a way that (Sobol, 1967);

$$\lim_{n\to\infty} \frac{1}{n} \sum_{i=1}^{n} f(x_i) = \int_{I^S} f \qquad (2)$$

Where x_i is a set of points uniformly distributed in a hypercube unit as H^n, like $x_i = (x_i^1, \dots, x_i^n)$. The inequality called Kosksma-Hlawka gives a higher bound for this integration error (Niederreiter, 1992),

$$\varepsilon \leq V(f) D_n \qquad (3)$$

V(f),s the variation of f(x) by the Hardy and Krause expression, and D_n function in which the first derivatives are continuous, V(f) is defined as the following expression (Niederreiter, 1992),

$$V(f) = \int_{H^*} |df(x)/dx| dx \qquad (4)$$

In higher dimensions, it will be possible to identify the durable-Krause variation in terms of partial derivatives. On the other hand, f(x) is assumed to be a function of limited change. Meanwhile, the smaller the discrepancy identified for the D_N, the better the integration convergence will be accessible. Therefore, convergence will be possible.

The design space was investigated with 100 samples. There are two design points that failed because of some geometric complication, but the rest of the design points were completed. In order to evaluate the performance of the GRS, the following output parameters were monitored to understand the degree of interactions between the hull, propeller and gate rudder:

Rudder parameters; $T_{GRS\ Total}$ (Total thrust on both rudders), F_Y (Side forces on each rudder separately)

Propeller parameters; $T_{Propeller}$ (Thrust on the propeller), Q (Torque on the propeller), N (Propeller rotation speed), J (Propeller advance coefficient) and P_D (Delivered power)

Hydrodynamic parameters; η_H, η_R, η_B, η_0, η_D are the Hull, relative-rotative, behind-hull, open-water and propulsion efficiencies, respectively. ω (wake fraction), t (Thrust deduction).

Although a best-performing design is chosen in Section 5, this paper does not contain any objective-based optimisation. Therefore, the best performing design chosen from the DoE study is not guaranteed that it is the best reachable design within the design space. The aim is to perform a sensitivity study to demonstrate a clear dependency level of the overall powering performance of the GRS over the geometrical design variables.

5 Results

The results of the DoE are presented in three sections in the following. The sensitivity results including the correlations graphs (Fig. 13 through Fig. **16**) are given in Section 5.1, the detailed resistance and propulsion investigations by

comparing the four selected cases are in Section 5.2, and the design validation results with SM method are included in Section 5.3.

5.1 Sensitivity Analysis

The DoE study was performed by creating 100 design points employing the earlier mentioned four geometrical parameters introduced in Section 2. There are 98 successfully completed nodes, while two design points failed because of a geometrical error.

This comprehensive sensitivity study determined the rudder angle as the most sensitive parameter.

Sasaki (2015) reported that the GRS has a strong interaction with the propeller as the rudders have higher flow velocity at their inner surfaces than the outers. This relation was clearly observed with the rudder's increasing angle of attack, i.e. “toe-in” position of the rudder leading edge (indicated by the negative “-“ sign) relative to the upstream flow. Therefore, unlike the conventional rudder systems, almost all design points have positive axial rudder force (i.e. thrust) within the solved design space, as shown in Fig. 13.

Contrary to expectations, high rudder thrust force does not decrease the propeller load. As shown in Fig. 14, the propeller thrust correlation with the rudder angle indicates that the propeller loads are maximum at rudder angles where the highest rudder thrust forces are recorded. Similarly, the delivered power correlation in Fig. 15 shows that the lowest power values are predicted at the rudder angles where low rudder thrusts are calculated.

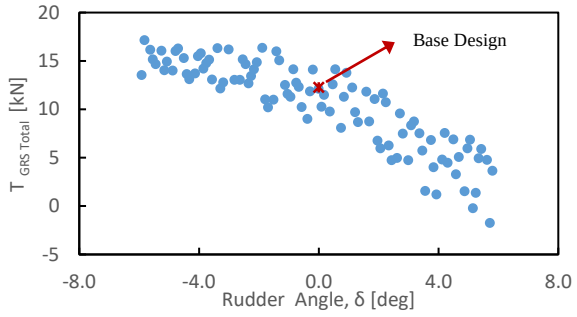

Fig. 13. Correlation graph of rudder angle, δ vs GRS Thrust Force

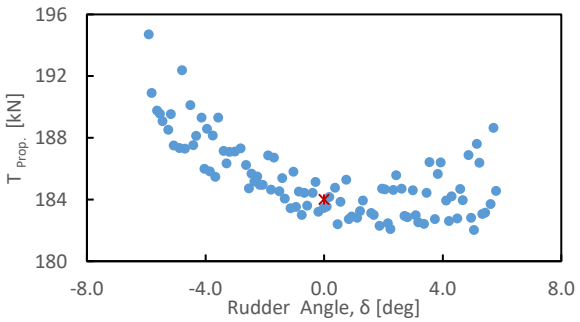

Fig. 14. Correlation graph of rudder angle, δ vs Propeller Thrust

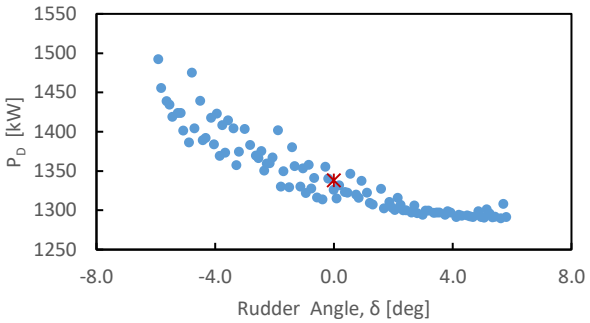

Fig. 15. Correlation graph of rudder angle, δ vs P_D

Regarding the rest of the design variables, there is a slightly positive correlation of the rudder X shift “dx” with the GRS thrust force, which means increasing dx values (in “+” direction) tends to give higher rudder thrusts, and a negative correlation with the propeller thrust. No significant effect is observed on the P_D. The correlation derivatives of the rudder tip skewness and the blade tip chord ratio are almost zero to the output parameters. Therefore these correlation graphs are not included in the paper.

In order to get a better understanding of GRS, further investigation was carried out over correlation graphs of the output parameters between one another. The P_D reaches the threshold between 0 to 6° rudder angle based on the current GRS propeller. No reduction in P_D was observed with decreasing rudder forces, as shown in Fig. 16. The minimum P_D was calculated at 1298.7 kW at Design Point 20 (DP20) with a 3.6% power reduction relative to the base design, which is indicated by a red cross (x) sign in the correlation graphs.

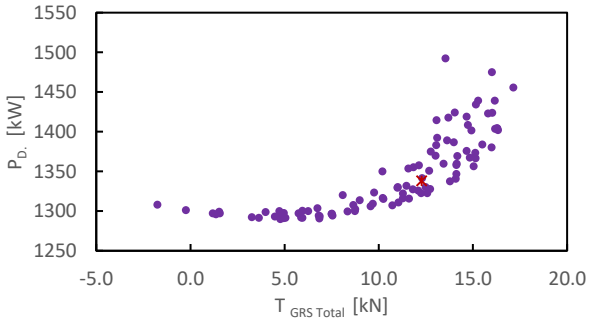

Fig. 16. Correlation between GRS thrust force vs P_D

5.2 Case-by-Case Investigation

A comprehensive comparison of hull, rudder and propeller forces were conducted over the four cases, which are: Bare Hull (without rudder system); Base (original) Design (BD); DP20, the chosen design point where the lowest shaft power was obtained within the design space; and DP50, the chosen design point where the highest gate rudder positive force was calculated

The case-by-case investigation is made for both towing and propulsion conditions described in the following.

5.2.1 Towing Condition

In order to present a physical insight to the effect of the design variables on the hydrodynamic interaction Fig. 18 is included

to present pressure coefficient variations at the aft end including the GRS blades in towing condition for the three design cases (ie. BD, DP20 and DP50) etc.

Based on the stern shape of the ship and local flow alignment with the gate rudder blade, the axial force on the rudder could change. Even with the higher rudder angle in the toe-in direction, axial rudder force can tend to be positive, as it is almost 0 resistance for DP50, which has a rudder angle of -5.8°. This phenomena is shown in Fig. 18, the stagnation point on the rudder is shifting outward from the leading edge of the rudder for DP50. On the contrary, the stagnation point moves inward of the blade leading edge for DP20 as it is more aligned with the flow. As a result, the rudder has significantly higher resistance relative to the BD and DP50 cases.

As it is for DP50, a higher toe-in angle could be considered an advantage in getting high positive rudder forces. However, the results in

Table **9** indicate that the Pressure Recovery Force (F_{PR}) shown in Eq 5 has more influence over the effective power.

$$F_{PR} = F_{H\,(App)} - F_{H\,(Bare)} \qquad (5)$$

Shifting the high-pressure region towards the leading edge or inner surface, the stern of the ship starts interacting with the rudders relatively in the positive pressure area. As a result, a higher pressure recovery force is obtained from the hull.

As shown in

Table **9**, the total rudder force (F_{GRS_T}) calculated on DP50 reduced significantly to -0.63 kN from -2.63 kN relative to BD, while it increased to -7.13 kN for DP20. On the contrary, the pressure recoveries are negative (additional resistance) for BD and DP50 at -1.46 and -9.28 kN, respectively. Meanwhile, the calculated F_{PR} for DP20 is positive (resistance recovery) at 3.34 kN, which means the F_H of DP20 is lower than the resistance of the bare hull.

To sum up, DP20 has a +0.33 kN additional resultant force (net force of F_{PR} and F_{GRS_T}) over BD, while DP50 has a -5.82 kN (extra resistance). The resistance advantage of DP20 can be seen in calculated effective power as well in

Table **9**. DP20 has slightly lower P_E at -0.2% over BD. Meanwhile, DP50 has a 3.7% higher effective power than BD.

5.2.1 Propulsion Condition

Similar investigations were conducted, including the action of the propeller in the propulsion condition. In this condition, unlike the calculated negative axial forces (resistance) on the rudders, there is a significant increment in the forces (i.e. developing positive thrust force) due to the effect of the propeller. As DP has a higher angle of attack, the rudder force ratio (F/T) of DP50 has the highest value of 9.0% among the results presented in

Table **9**. Because of its more inline with the incoming flow, DP20 has the lowest F/T of 2.6%, while BD has a value of +6.8%.

Similar to the towing condition, the pressure recovery was found to be significantly higher for DP20. While the pressure recovery rates are negative for the DP50 and BD cases, displaying an extra 18.56 kN and 6.81 kN resistance values (equal to F/T values of -9.7% and -3.7%, respectively), the DP20 case displays a pressure recovery of 1.0 kN, (i.e., F/T of 0.6%). The resultant force for DP20 is 0.32 kN and 7.18 kN higher than the BD and DP50 cases, respectively.

As shown in

Table **9**, there is a 3.6% saving in P_D calculated for the DP20 relative to the BD case. The P_D for DP20 is even 0.8% lower than the P_D for the Bare Hull case. DP50, the design with the highest $F_{GRS\,T}$, presents 1455 kW of P_D, which is 8.8% higher than the BD case.

The force distributions along the gate rudder blade (height or span) in terms of the pressure coefficients are given in Fig. 19 for the BD, DP20 and DP50 cases at both towing and propulsion conditions. The vertical part of the rudder is divided into eight equal sections starting from the blade tip at the bottom) to the rudder stock at the top. The shoulder and upper sections are kept in separate parts, which are parts 9 and 10, respectively, for the force discretisation. It is clearly seen that the DP20's force distribution is significantly lower than other designs, as shown in Fig. 19. However, especially the calculated values at the blade tip region (part 1) are similar to the BD case, while it has the weakest blade tip vortex. The reason is that the DP20 is more aligned with the flow, and hence the tip vortex and force (thrust) reduction are relatively less than the other two designs, as can be shown in Fig. 20**.** Especially, DP50 has the strongest tip vortex structure and, as a result, the dramatic force reduction at the blade tip.

From Table 7, behind hull efficiency (η_B) is the highest at DP50 since the propeller's operation point is at a favourable advance coefficient of J = 0.58, while others are at less favourable smaller Js as shown in Table 9. Although the propeller efficiency for the DP50 case is higher than the rest of the design cases, it is still the least favourable design in terms of the delivered power. It means the significant difference comes from the hull efficiency (η_H), which is a function of the thrust deduction fraction (t) and wake fraction (ω) as given in Eq. 6.

$$\eta_H = \frac{1-t}{1-\omega} \qquad (6)$$

Here the thrust deduction (t) is not changing based on the GRS rudder design or rudder angle for the investigated cases. Therefore, it is necessary to give a clear answer to the question of how the power requirements are -3.6% for the DP20 and +8.8% for the DP50 case relative to the BD case, while the propeller thrusts are only -0.2% and +4.8% of the BD's thrust.

As shown in Table 7, DP20 is the GRS design case with the highest η_H =1.24. while the contributing values of ω and t are similar for the three selected GRS design cases. The highest calculated ω is 0.305 for DP20 within the three design cases. This means there is a relatively lower velocity at the propeller cross-section. As a result, there is higher static pressure (as shown in Fig. 18) and higher η_H. Also, the correlation graphs for the wake and P_D give a global indication which shows that lower P_D is calculated with a higher wake fraction, as shown in Fig. 17.

Table 7. Non-dimensional coefficients for the chosen cases

Case	t	ω	η_0	η_R	η_B	η_H	η_D
Bare Hull	0.181	0.344	0.59	1.003	0.59	1.25	0.74
Base Design	0.135	0.261	0.63	1.000	0.63	1.17	0.73
DP20	0.135	0.305	0.61	1.002	0.61	1.24	0.76
DP50	0.135	0.210	0.64	0.997	0.64	1.09	0.70

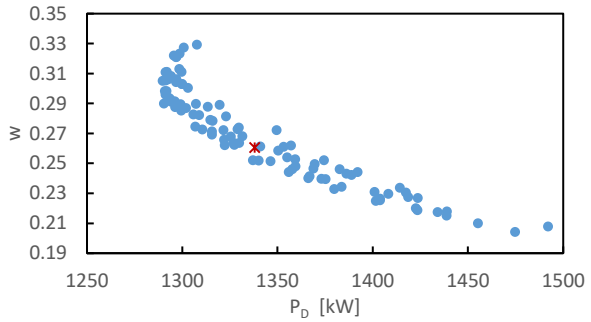

Fig. 17. Correlation between GRS thrust force vs P_D

5.3 Design Validation

As stated earlier, the simplified approach was used for both modellings of the fluid domain and propeller (using VD) in the DoE study and the case-by-case comparisons. However, here in the design validation study, the full domain was modelled by employing the SM approach in order to make sure that predicted power in DoE saving was met with high the fidelity CFD calculation.

The force variables are compared between the BD and DP20 cases in Table 8. With the more comprehensive design validation case, an additional 1.6% per cent reduction in P_D was calculated. As a result, the optimum rudder design, at the optimum rudder angle, provides a 5.2% power saving relative to the base design. For further information the powering performance parameters for CRS are also included in Table 8.

Table 8. High fidelity CFD results for CRS, GRS BD and DP20

	CRS	GRS BD	GRS DP20	$\delta\emptyset_{DP20\ vs\ BD}$
T, N	212.2	189.0	187.4	-0.8%
Q,kN.m	98.1	93.8	91.3	-2.6%
N, rpm	151.5	136.8	133.20	-2.6%
P_D, kW	1556	1344	1274	-5.2%
$R_{GRS\ PRT}$, kN	-	6.3	1.9	-70.5%
$R_{GRS\ STB}$, kN	-	5.1	1.6	-69.3%

Table 9. Forces and power values for different cases

Case	F_{Ship} (kN)	F_H (kN)	F_{PR} (kN)	F_{GRS_T} (kN)	T (kN)	Q (kN.m)	N (RPM)	J [1]	w [1]	t [1]	P_E kW	P_D kW
Bare Hull (T)	-155.17	-155.17	-	-	-	-	-	-	-	-	958	-
(P)	-189.50	-189.50	-	-	189.51	95.10	130.5	0.517	0.344	0.181	-	1300
Base Design (T)	-159.26	-156.63	-1.46	-2.63	-	-	-	-	-	-	983	-
(T)	-184.04	-196.31	-6.81	12.27	184.01	94.69	134.9	0.564	0.261	0.135	-	1338
DP20 (T)	-158.93	-151.80	3.38	-7.13	-	-	-	-	-	-	981	-
(P)	-183.72	-188.50	1.00	4.78	183.71	93.41	131.8	0.542	0.305	0.135	-	1290
DP50 (T)	-165.08	-164.45	-9.28	-0.63	-	-	-	-	-	-	1019	-
(P)	-190.09	-208.06	-18.56	17.16	190.90	99.27	140.0	0.581	0.210	0.135	-	1455

Towing Condition

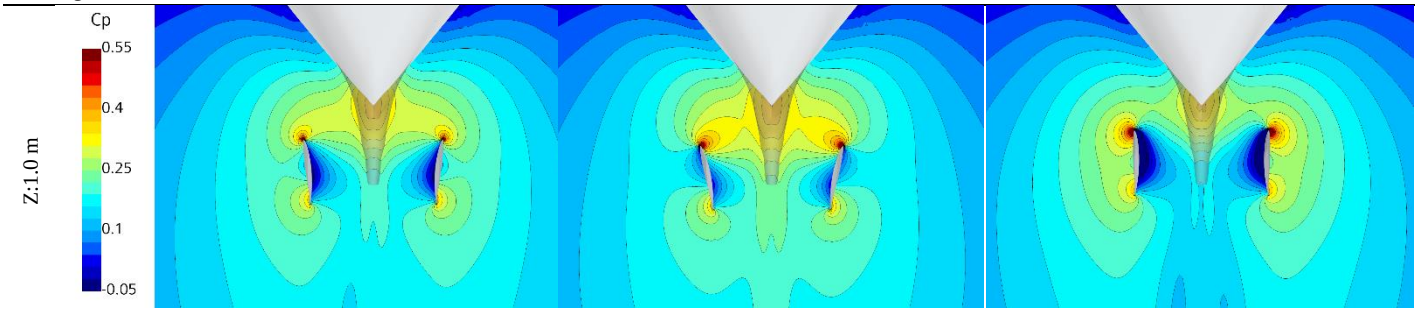

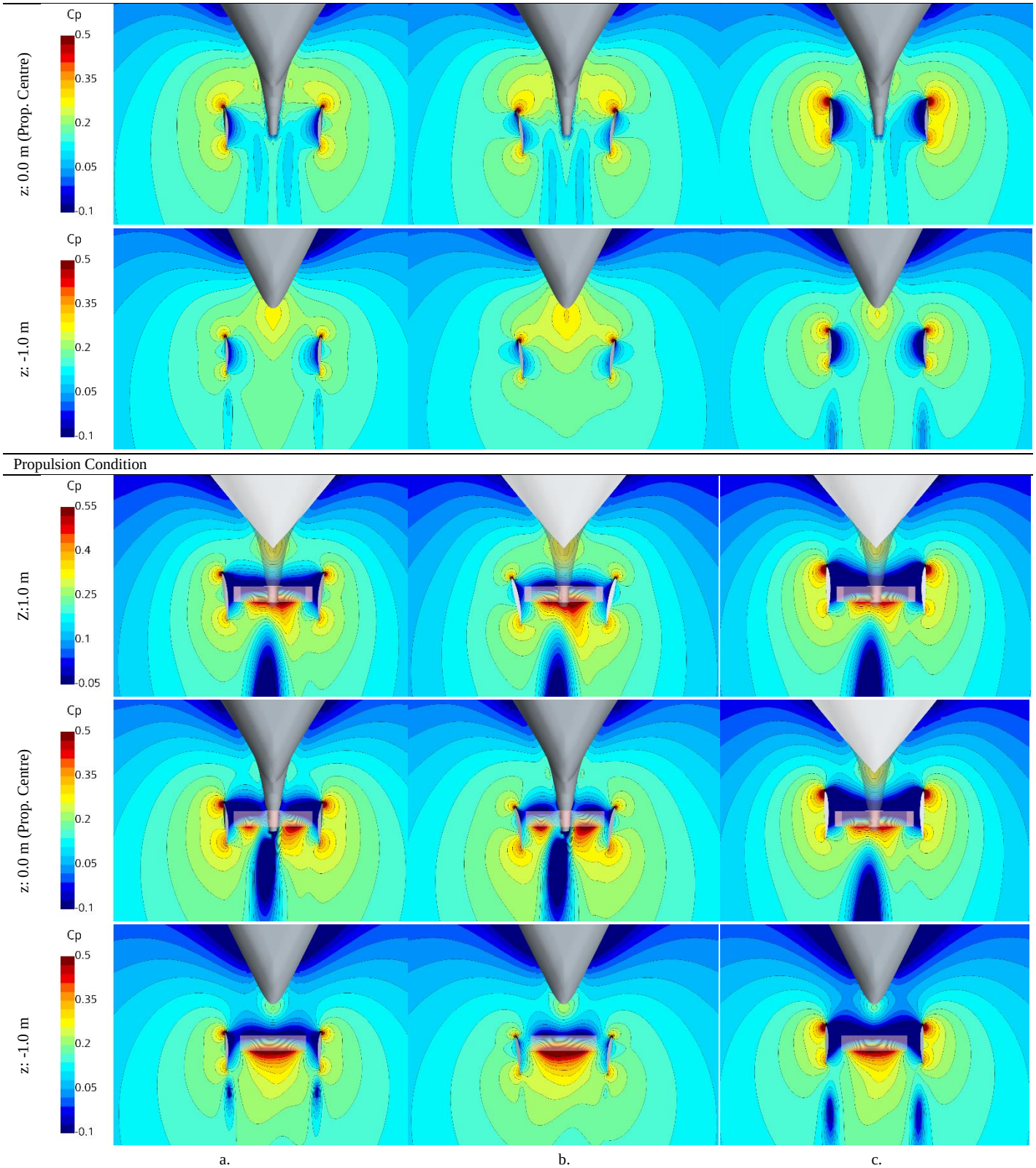

Fig. 18. Pressure coefficient at the stern of the ship at different horizontal sections; a.BD, b.DP20, c.DP50

Towing Condition

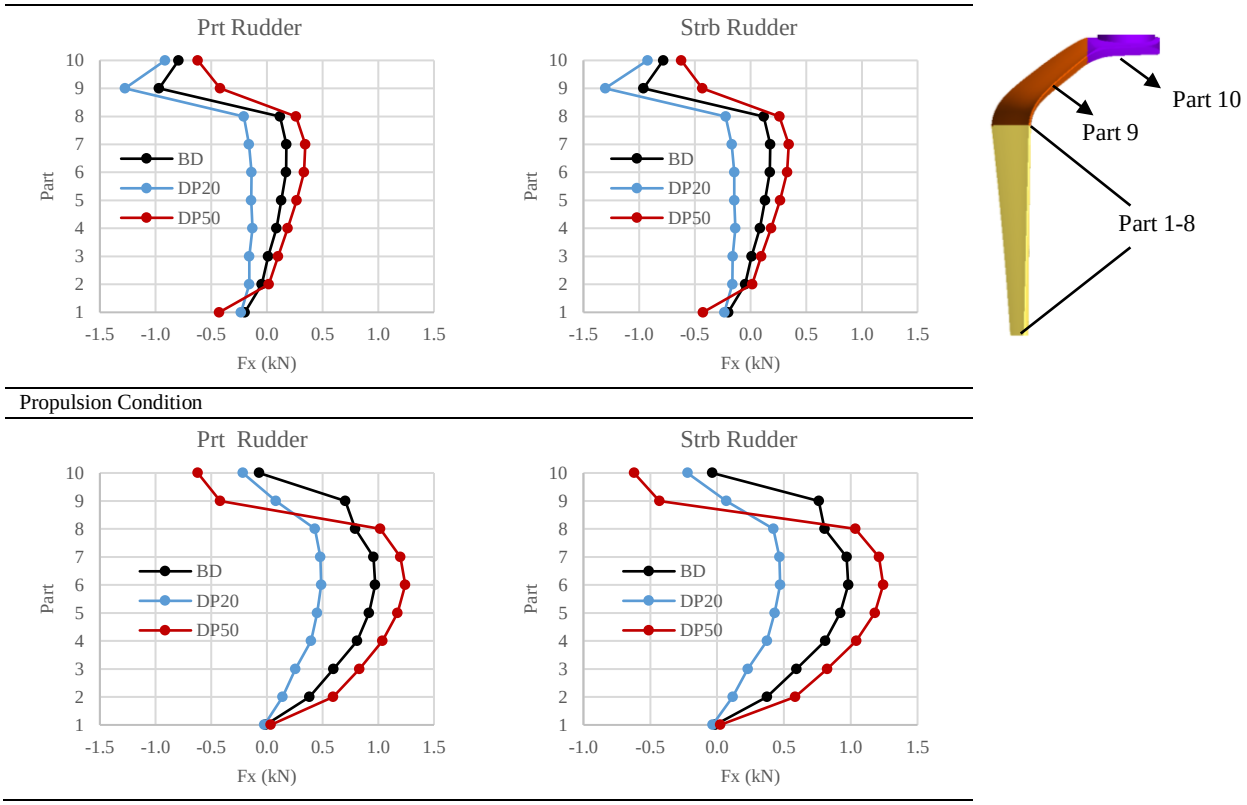

Fig. 19. Pressure coefficient along the gate rudder height at different horizontal sections; a.BD, b.DP20, c.DP50

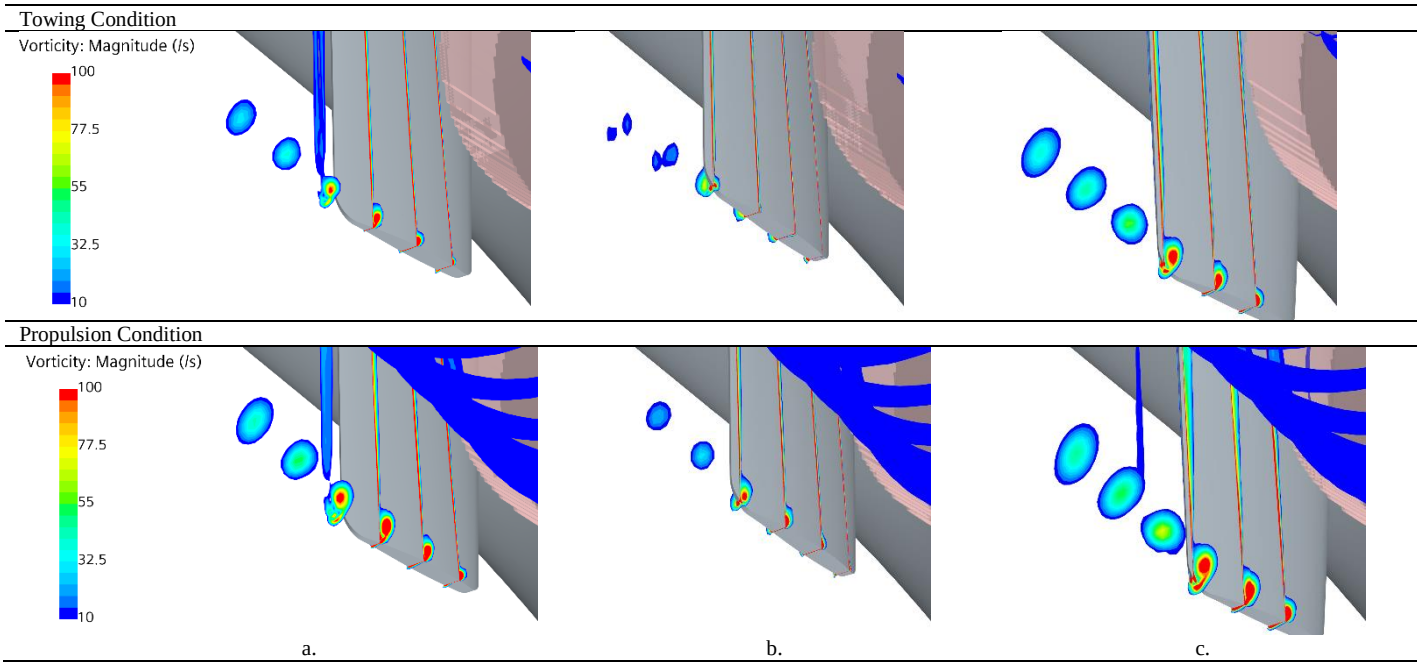

Fig. 20. Vorticities at rudder tip region; a.BD, b.DP20, c.DP50

6 Conclusions

The main objective of this paper is to provide a design/optimisation perspective for the GRS design methodology development in the GATERS project.

In order to determine the critical (fundamental) design parameters for the GRS influencing the ship's powering performance, the DoE approach based on the Sobol Algorithm can be effective.

Based on the DoE set-up conducted and applied on a 90m cargo vessel in this study, the most critical GRS design parameter was found to be the rudder angle. With an optimised rudder angle, the propulsion performance of the GRS can be improved by decreasing the power requirement around 5%. In this study, it was proved that improvement in power saving relative the CRS is for 13.7% for BD while this saving become 18.1% for DP20 by means of DoE. Indeed, a further improvement would also be possible with a new wake-adapted propeller design.

Although the positioning of the GRS relative to the propeller could be another influential design parameter to explore, this may be constrained probably by the steering room arrangement, especially for retrofit GRS design cases.

However, the main design objective for the best GRS design should not be the GRS thrust force. Instead, powering performance could be optimised by maximising the wake fraction and pressure recovery through the mutual interaction amongst the aft end, propeller and gate rudder blades.

7 References

Agreement, G. (2020). *GATERS-H2020-MG-2018-2019-2020/H2020-TwoStages - No: 860337*. The European Commissions .

Carchen, A., Turkmen, S., Piaggio, B., & Shi, W. (2020). Investigation of the manoeuvrability characteristics of a Gate Rudder system using numerical, experimental, and full-scale techniques. *Applied Ocean Research*.

Carchen, C., Shi, W., Sasaki, N., & Atlar, M. (2016). A prediction program of manoeuvrability for a ship with a Gate Rudder system. *2nd International Meeting on Recent Advances in Prediction Techniques for Safe Manoeuvring of Ships and Submarines.* Istanbul.

Celik, I. B., Ghia, U., Roache, P. J., Freitas, C. J., Coleman, H., & Raad, P. E. (2008). Procedure for estimation and reporting of uncertainty due to discretization in CFD applications. *Journal of Fluids Engineering-Transactions of the ASME 078001-078001-4 , 130*((7)).

Celik, I. B., Ghia, U., Roache, P. J., Freitas, C. J., Colmena, H., & Raad, P. E. (2008). Procedure for estimation and reporting of uncertainty due to discretization in CFD applications. *Journal of Fluids Engineering-Transactions of the ASME 0078001-078001-4*, 130((7)).

FSYS. (2022, November). *CAESES*. Retrieved from Friendship System: https://www.caeses.com/about-us/

IMO. (2018). *Adoption of the initial IMO strategy on reduction of GHG emissions from ships and existing IMO activity related to reducing GHG emissions in the shipping sector*. International Maritime Organization.

ITTC. (2014). *Partical Guidelines for Ship Self-Propulsion CFD.*

Navid, A., Khalilarya, S., & Abbasi, M. (2018). Diesel engine optimization with multi-objective performance characteristics by non-evolutionary Nelder-Mead algorithm: Sobol sequence and Latin hypercube sampling methods comparison in DoE process. *Fuel*, 349-367.

Niederreiter, H. (1992). Random number generation and quasi-Monte Carlo methods. *Soc.for Ind. and Appl. Math*.

Richardson, L. F. (1911). The approximate arithmetical solution by finite differences of physical problems involving differential equations, with an application to the stresses in a masonry dam. *Transactions of the Royal Society of London, 210*(459-490).

Richardson, L. F., & Gant, J. A. (1927). The deferred approach to the limit. *Transactions of the Royal Society of London, 226*(636-646).

Richardson, L. F., & Gant, J. A. (1927). The deferred approach to the limit. *Transactions of the Rotal Society of London*, 266(636-646).

Sasaki, N., Atlar, M., & Kuribayashi, S. (2015). Advantages of twin rudder system with asymmetric wing section aside a propeller. *Journal of Marine Science and Technology*.

Sasaki, N., Kuribayashi, S., & Miles, A. (2019). Full scale performance of gate rudder. *Propellers & Impellers – Research, Design, Construction & Applications*. London.

Sasaki, N., Kuribayashi, S., Atlar, M., & Fukazawa, M. (2020). Towards a realistic estimation of the powering performance of a ship with a gate rudder system. *Journal of Marine Science and Engineering*.

Sobol, I. (1967). Distribution of points in a cube approximate evaluation of integrals. *U.S.S.R. Comput. Maths. Math. Phys. 7 (in English)*, 86-112.

StarCCM+. (2022, November). *Star CCM+*. Retrieved from Siemens: https://www.plm.automation.siemens.com/global/en/products/simcenter/STAR-CCM.html

Turkmen, S., Carchen, A., Sasaki, N., & Atlar, M. (2016). A New Energy Saving Twin Rudder System - Gate Rudder. *International Conference on Shipping in Changing Climates (SCC 2015).* Glasgow.